Article

Exploring Rapid Photocatalytic Degradation of Organic Pollutants with Porous CuO Nanosheets: Synthesis, Dye Removal, and Kinetic Studies at Room Temperature

Mohammed Nazim,* Aftab Aslam Parwaz Khan, Abdullah M. Asiri, and Jae Hyun Kim*

Read Online

ACCESS | Metrics & More | Article Recommendations | Supporting Information

ABSTRACT: In this work, we report the facile, environmentally friendly, room-temperature (RT) synthesis of porous CuO nanosheets and their application as a photocatalyst to degrade an organic pollutant/food dye using $NaBH_4$ as the reducing agent in an aqueous medium. Ultrahigh-resolution field effect scanning electron microscopy images of CuO displayed a broken nanosheet-like (a length of ~160 nm, a width of ~65 nm) morphology, and the lattice strain was estimated to be ~1.24×10^{-3} using the Williamson−Hall analysis of X-ray diffraction plots. Owing to the strong quantum size confinement effect, CuO nanosheets resulted in an optical energy band gap of ~1.92 eV, measured using Tauc plots of the ultraviolet−visible (UV−vis) spectrum, resulting in excellent photocatalytic efficiency. The RT synthesized CuO catalyst showed a high Brunauer−Emmet−Teller surface area of 30.88 ± 0.2313 m^2/g (a correlation coefficient of 0.99972) with an average Barrett−Joyner−Halenda pore size of ~20.385 nm. The obtained porous CuO nanosheets exhibited a high crystallinity of 73.5% with a crystallite size of ~12 nm and was applied as an efficient photocatalyst for degradation of the organic pollutant/food dye, Allura Red AC (AR) dye, as monitored by UV−vis spectrophotometric analysis and evidenced by a color change from red to colorless. From UV−vis spectra, CuO nanosheets exhibited an efficient and ultrafast photocatalytic degradation efficiency of ~96.99% for the AR dye in an aqueous medium within 6 min at RT. According to the Langmuir−Hinshelwood model, photodegradation reaction kinetics followed a pseudo-first-order reaction with a rate constant of $k = 0.524$ min^{-1} and a half-life ($t_{1/2}$) of 2.5 min for AR dye degradation in the aqueous medium. The CuO nanosheets showed an outstanding recycling ability for AR degradation and would be highly favorable and an efficient catalyst due to the synergistic effect of high adsorption capability and photodegradation of the food dye.
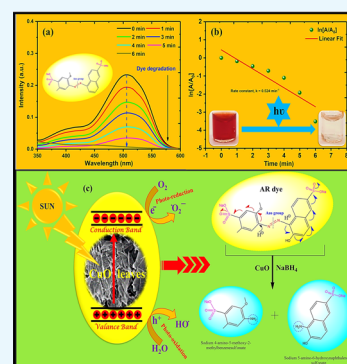
INTRODUCTION

Environmental pollution including air, water, and soil pollution is a global issue that seriously endangers the health of this planet's organisms, including human beings.[1,2] Various efforts have been undertaken to develop efficient, environmentally friendly, and low-cost methods for removing organic dyes/pollutants from water.[3,4] Transition-metal oxides are considered to be the most promising catalysts for cleaning wastewater in a facile, reliable, quick, and eco friendly way because of their high photocatalytic activity, excellent solubility, and stability.[5,6] Organic dyes and pigments are considered the most common sources of water pollutants in various sectors, including textile, leather, paper, cosmetics, paint, and printing industries.[7,8] In particular, textile industrial dye stuffs contain several toxic organic components and are major contributors (~20%) to total water pollution among paints, food dyes, food colorants, etc.[9,10]

Organic dyes/pollutants with azo (−N≡N−) groups and naphthalene or benzene rings account for the largest part (>50%) of all industrial organic water pollutants.[11,12] Various food ingredients make food products more attractive and appealing without any improvement in their nutritional values.[13−15] Additionally, azo dyes can be reduced to form various amine derivatives which might cause harmful effects and develop a number of health problems, especially in children, such as allergies, immune suppression, urinary problems, and DNA damage.[16−18] The Allura Red AC (AR) (chemical Formula: $C_{18}H_{14}N_2Na_2O_8S_2$, molecular weight: 496.4) dye is a synthetic food coloring agent, widely employed in food products, medications, and cosmetics as well as different meat and fish products, chewing gum, soft drinks, jellies and jams, canned food, and various bakery and dairy products.[19,20]

With excess consumption, the AR dye might be harmful to humans and might cause cancer based on World Health Organization (WHO) toxicological data.[21−23] According to the US Food and Drug Administration (FDA), the AR dye has shown potential toxicity and carcinogenic effects, and it is presently banned in Belgium, Switzerland, France, and Denmark
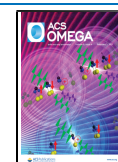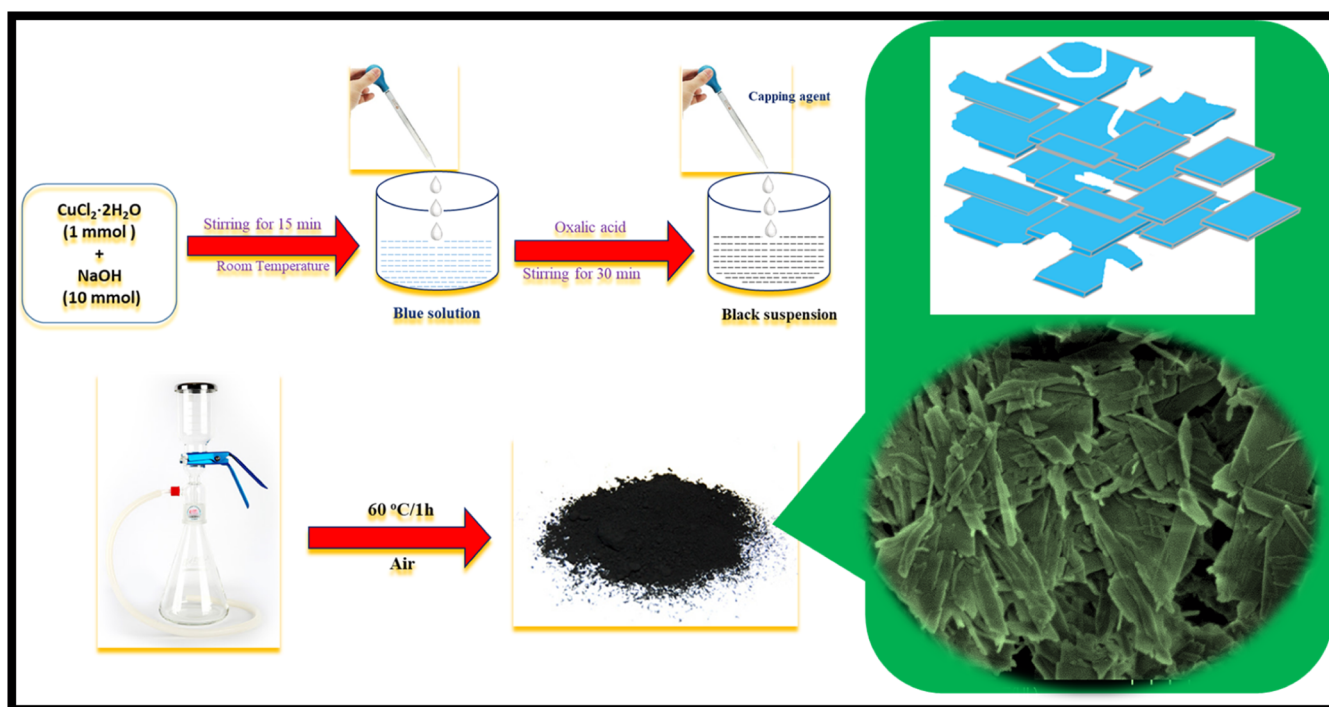
Figure 1. Stepwise synthesis protocol of CuO nanosheets at RT.

and not recommended for children in the United Kingdom.[24] Azo dyes exhibit amphoteric properties and explore anionic properties by deprotonation at the acidic group, cationic properties by protonation at the amino group, or non-ionic properties as a function of pH due to the presence of carboxyl, hydroxyl, amino, or sulfoxyl groups.[25]

Being a p-type semiconductor, cupric oxide (CuO) nanomaterials are considered as highly promising materials for applications in diverse fields including semiconductors, memory devices and field-effect transistors, solar energy, lithium-ion batteries, and photocatalysts for degradation of organic pollutants.[26−28] Depending on their particular synthetic protocols (Figure 1), CuO nanomaterials obtain various morphological shapes as nanowires, nanoflowers, nanoplates, nanoboats, and ellipsoid forms, which can greatly influence their photodegradation efficiency toward azo dyes in aqueous media.[29,30] CuO nanomaterials possess a monoclinic crystalline structure with a large surface area, high thermal conductivity, high stability, and antimicrobial activity.[31] CuO has a monoclinic structure where each Cu atom contains four nearest neighbor oxygen atoms and exists at the center of the oxygen rectangle, while oxygen atoms are located at the center of a distorted tetrahedron of Cu atoms.[32]

In this work, we report a facile, room-temperature (RT) synthesis of CuO broken nanosheets as an efficient photocatalyst for speedy degradation of the organic pollutant/food dye, AR, in aqueous media. The as-prepared CuO nanosheets were thoroughly characterized by high-resolution powder X-ray diffraction (HR-XRD), X-ray photoelectron spectroscopy (XPS), ultrahigh-resolution scanning electron microscopy (UHR−SEM), high-resolution transmission electron microscopy (HR-TEM), and ultraviolet−visible (UV−vis) absorption spectroscopy. From UV−vis absorption spectra, as-prepared CuO nanosheets exhibited a strong confinement and size effect, with a high energy band gap, compared to bulk CuO nanomaterials. The ultrafast catalytic degradation of the AR

dye was achieved in an aqueous solution in the presence of NaBH$_4$ as a reducing agent. The as-prepared CuO broken nanosheets attained >96% photodegradation efficiency within 6 min at RT under UV light irradiation.

RESULTS AND DISCUSSION

Ultrahigh-Resolution Field Effect SEM. To determine the size and morphology of CuO powder, ultrahigh-resolution field effect SEM (UHR−FESEM) images (Figure 2a,b) with their corresponding elemental mapping images were obtained at different magnifications. The porous morphology of the synthesized CuO is revealed, composed of torn or broken sheets with different sizes and an average length of ∼100−160 nm, a thickness of ∼15 nm, and a width of 25−65 nm. During synthesis, the nanosheet formation process is initiated by the nucleation of nanorods, followed by accumulation or aggregation of multiple CuO nanorods via self-assembly behavior.[33,34] The corresponding element mapping images (Figure 2c,d) clearly exhibit the existence of the Cu and O elements and the homogeneous dispersion of the Cu and O elements throughout the nanosheets. The analyses of the CuO nanosheet length and width are shown in the histogram profile (Figure 2e,f) with standard deviation analysis.

High-Resolution Transmission Electron Microscopy. The TEM image (Figure 2g) of CuO exhibits various types of CuO nanosheets, which resemble broken nanosheets of about >100 nm lengths. From lattice fringes, CuO nanosheets have a highly crystalline broken sheetlike morphology, and the *d*-spacing of crystallographic planes was calculated using fast Fourier transform (FFT) patterns to be ∼0.45 nm, which is consistent with (111) crystal planes of monoclinic-phase CuO nanomaterials.[35] The typical TEM images of as-prepared CuO nanostructures demonstrate a broken sheetlike morphology and support surface structure observed by UHR−FESEM analysis.

Energy-Dispersive X-Ray Spectroscopy. The elemental composition and phase purity of CuO nanosheets were further
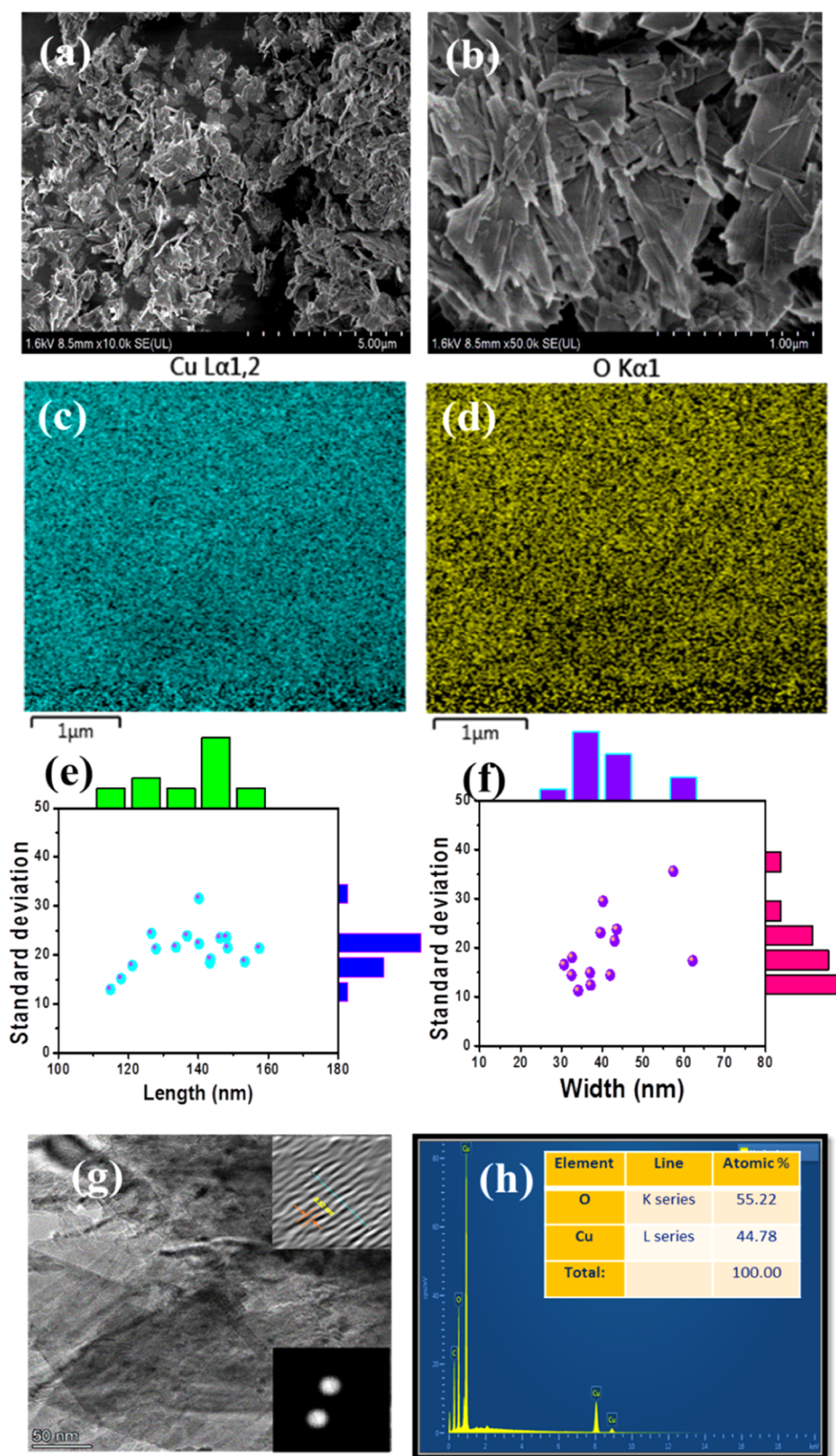
Figure 2. UHR−FESEM images of CuO nanosheets; (a) low-magnification and (b) high-magnification images with elemental mapping of (c) Cu element and (d) O element. (e) CuO nanosheet width histogram profile with standard deviation. (f) CuO nanosheet length histogram profile with standard deviation. (g) HR−TEM image of CuO broken nanosheets with FFT patterns. (h) EDX spectral (inset: atomic percentage of elements) plot of CuO nanosheets.

analyzed by energy-dispersive X-ray (EDX) analysis. The EDX spectra (Figure 2h) of CuO nanosheets showed the presence of

only Cu and O as major components at a molecular ratio of Cu/ O (1:1), which is in agreement with the stoichiometric
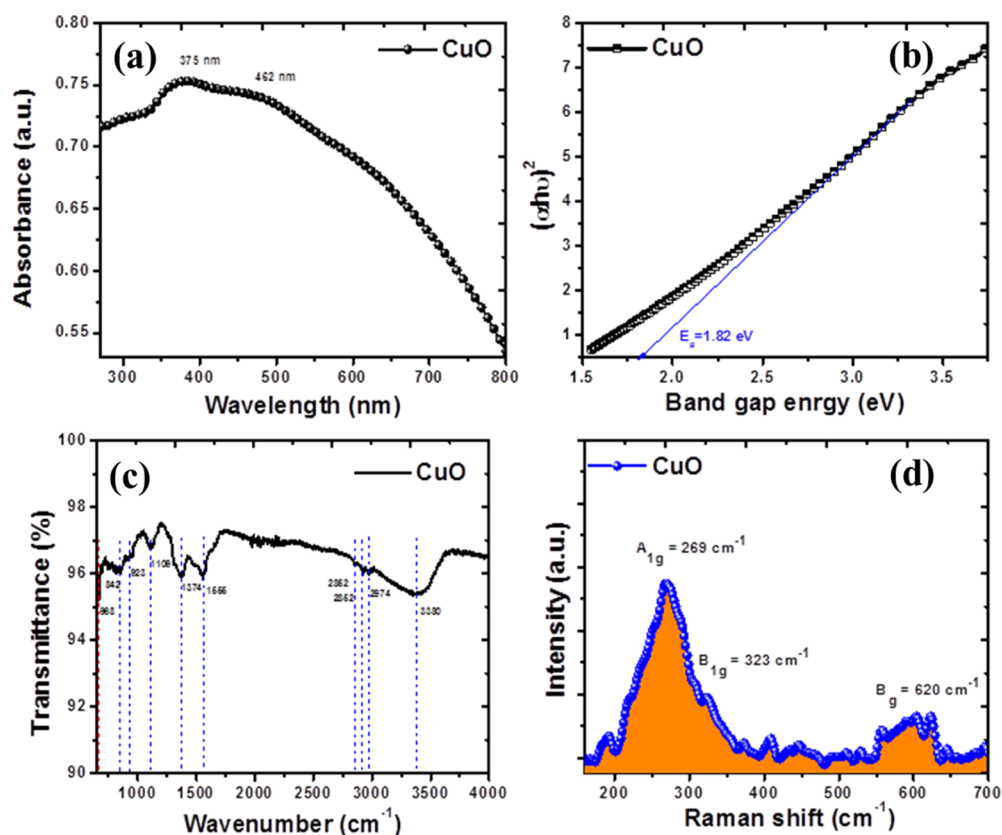
Figure 3. (a) UV−vis spectrum and (b) corresponding Tauc plot of CuO nanosheets; (c) FT-IR spectrum; (d) FT-Raman spectrum of RT synthesized CuO nanosheets.

proportion of CuO in the Cu^{2+} oxidation state. Furthermore, the CuO nanosheet powder also contains some carbon byproducts from the organic precursor along with the main Cu and O elements.[36]

Optical Properties of Porous CuO Nanosheets. In photocatalysis, the optical band gap of the transition-metal oxide plays a very significant role in determining light harvesting ability. In UV−vis spectral (Figure 3) plots, CuO nanosheets have shown two peaks at ~375 and ~462 nm. In general, reduction in nanoparticle size improves not only the band gap but also the surface area of CuO nanosheets, leading to more efficient photodegradation performance.

Lowering the size of nanomaterials leads to a small charge diffusion length, which minimizes the charge-recombination process due to rapid charge transfer, resulting in improved photocatalytic efficiency (PE).[37] The optical energy band gap of RT synthesized CuO nanosheets was estimated by the Tauc plot (Figure 3b), where the $(\alpha h\nu)^2$ versus $h\nu$ plot can be used in following equation

$$(\alpha E_{\text{photon}})^2 = K(E_{\text{photon}} - E_{\text{g}}) \qquad (1)$$

where α is the absorption coefficient, $E_{\text{photon}} = h\nu$ is the photon energy, K is a constant, and E_{g} is the optical energy band gap. The estimated optical energy band gap ($E_{\text{g}} = 1240/\lambda_{\text{edge}}$) of CuO broken nanosheets was about ~1.92 eV, which is much larger than that of bulk CuO (~1.20 eV) crystals.[38] The high band gap of RT synthesized CuO nanosheets is attributed to quantum size confinement effects which result from the nanosized morphology of metal oxide semiconducting materials resulting in size-dependent optical properties.

Fourier Transform Infrared Spectroscopy. The Fourier transform infrared (FT-IR) spectra (Figure 3c) of CuO nanosheets show a broad and high frequency band at 3382 cm^{-1}, corresponding to the hydroxyl (OH) functional group of the capping agent applied during synthesis. Along with this, three characteristic alkane C−H stretching bands appeared at 2974, 2852, and 2783 cm^{-1}. Additionally, broad IR frequency bands in the range of ~1300 to ~4000 cm^{-1} are assigned to chemisorbed and/or physisorbed H_2O and CO_2 molecules on the surface of CuO nanosheets. In the IR spectrum, the sharp band at ~1374 cm^{-1} is assigned to the C−H deformation vibration of alkanes, along with a strong band at ~1555 cm^{-1} corresponding to C=O stretching vibrations of carboxylic groups.[39] The band at ~1109 cm^{-1} is assigned to the C−O−C antisymmetric stretching vibration band of carboxylic acid groups of oxalates. The IR bands in the frequency range of ~1000 to 700 cm^{-1} in the fingerprint region are attributed to the C−O stretching and in-plane C−H bending vibrations. Furthermore, the peak at ~923 cm^{-1} is assigned to the bending vibration of the C−H group, and the frequency band of ~842 cm^{-1} is attributed to the bending vibrations of O−M−O bonds. However, the characteristic peak at a low frequency of ~668 cm^{-1} corresponds to the typical Cu−O stretching vibration band.[40]

Fourier Transform Raman Spectroscopy. Raman spectroscopy is a very useful tool for monitoring the structural disorder and crystalline nature of various metal oxide materials at RT. FT-Raman spectroscopy provided further evidence of the monoclinic crystal phase (Figure 3d) of CuO nanosheets. FT-Raman spectral plots exhibited three strong peaks at 270, 335, and 597 cm^{-1}, which were assigned to the monoclinic
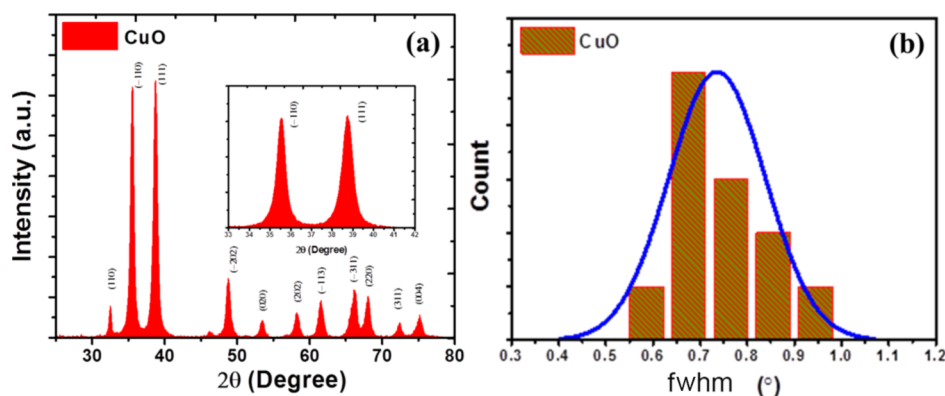
Figure 4. (a) Powder XRD spectrum and (b) histogram profile of fwhm of RT synthesized CuO nanosheets.

orientation of A_{1g}, B_{1g}, and B_g vibrational modes of CuO nanosheets, respectively.[41] From the Raman spectrum, a peak around ~100 cm^{-1} might have appeared due to Raman scattering at the edge due to vibrations induced by disorder or by an impurity that became Raman-active owing to breakage of selection rules. Crystal lattice imperfections and oxygen deficiencies resulting from the impurity might broaden Raman peaks as the grain size of metal-oxide nanomaterials decreases. The broadened peaks of XRD and Raman spectra indicate a small size of CuO nanoparticles which agglomerate to form porous CuO nanosheets.[42]

Powder X-ray Diffraction Spectroscopy. Powder XRD (Figure 4) was applied as a precise and efficient tool to investigate the crystalline phase and size of CuO nanostructures. The diffraction peaks of CuO nanosheets were at Bragg angle (2θ) values of 32.536, 35.584, 38.768, 48.813, 53.453, 58.243, 61.566, 66.143, 68.074, 72.451, and 75.222°, which belong to the crystal plane indices of the (110), (002)/(−111), (111), (−202), (020), (202), (−113), (−311), (220), (311), and (−222) phases, respectively. The XRD peaks reveal a monoclinic crystalline phase ($\alpha = \gamma = 90°$ and $\beta = 99.5°$) of CuO (space group C_{12}/C_1, JCPDS no. 98-008-7124) with lattice constants of $a = 4.687$, $b = 3.422$, and $c = 5.130$ Å at RT. The XRD results indicate that as-obtained CuO nanosheets are composed of a pure monoclinic crystal phase with a full width at half-maximum (fwhm) value of 0.74 nm, obtained by using Gaussian fit curves.[43] Additionally, the degree of crystallinity (Table 1) indicates positions of various atoms or molecular

Table 1. Structural Parameters of RT Synthesized CuO Nanosheets

material	wavelength (nm)	energy band gap (eV)	crystallite size (nm)	fwhm (deg)	strain (ε)
CuO nanosheets	375,462	1.92	12	0.72	1.24×10^{-3}

arrangements in powder materials, which can be calculated using the following relation

$$\text{Crystallinity (\%)}$$
$$= \frac{\text{total area of crystalline peaks}}{\text{total area of all (crystalline and amorphous) peaks}}$$
$$\times 100 \tag{2}$$

The RT synthesized CuO nanosheets exhibited ~73.5% crystallinity, suggesting the high crystalline nature of the CuO photocatalyst which is beneficial to rapid dye degradation.

From XRD plots, the crystal orientation of CuO and the crystallite grain size of CuO nanosheets were calculated using the Debye−Scherrer formula

$$D = K\lambda/\beta \cos \theta \tag{3}$$

where D is the crystallite size, K is the shape factor (0.9), λ is the X-ray wavelength, β is the fwhm, and θ is the Bragg angle of the XRD peak. The average crystallite size (D_{average}) of CuO nanosheets was estimated to be ~12 nm (Table 1) for degradation of the organic pollutant at RT.

Among solid nanomaterials, XRD peak broadening might be attributed to the presence of an impurity in the crystal lattice, which creates defects infinitely in all the directions. The fwhm value (Figure 4b) was estimated to be 0.72 for CuO broken nanosheets. The Williamson−Hall (W−H) analysis suggests the XRD peak-width relation with the XRD intensity of 2θ peak positions for calculating the lattice strain, according to the equation

$$\beta \cos \theta = (k\lambda/D) + 4\varepsilon \sin \theta \tag{4}$$

where ε is the lattice strain, D is the particle size, β is the peak broadening at the fwhm value of the CuO powder, λ is the X-ray wavelength, k is a constant, and θ is Bragg's angle. From the W−H plot (Figure S1), the calculated strain of CuO nanosheets was found to be 1.24×10^{-3} at RT.

X-ray Photoelectron Spectroscopy. The chemical constituents of CuO nanosheets with their oxidation states were analyzed by XPS spectral plots. For CuO, XPS spectra (Figure 5) were used to investigate transition-metal compounds with localized valence d-orbitals, and copper metal ($_{29}$Cu in the d^{9}s^2 configuration) exists mainly in the divalent oxidation state (Cu^{2+} ion) with the d^9 configuration. The Cu 2p spectrum (Figure 5a) displays two sharp and distinctive peaks of Cu 2p$_{3/2}$ and Cu 2p$_{1/2}$ oxidation states, with their corresponding strong shake-up satellite peaks, indicating the coexistence of two forms of Cu^{2+} ions in nonequivalent chemical environments.[44]

The Cu 2p$_{3/2}$ peak was situated at 933.80 with its asymmetric satellite shoulder peaks at 941.00 and 943.80 eV, corresponding to the Cu^{2+} oxidation state of CuO nanosheets. In addition, the satellite peak at 943.80 eV provides an evident proof of the d^9 shell of the Cu^{2+} state, which is a characteristic of copper oxide materials with a d^9 configuration in the ground state.[45] Additionally, the Cu 2p$_{1/2}$ peak of CuO was situated at 953.67 eV with the corresponding shake-up satellite peak at 962.33 eV,
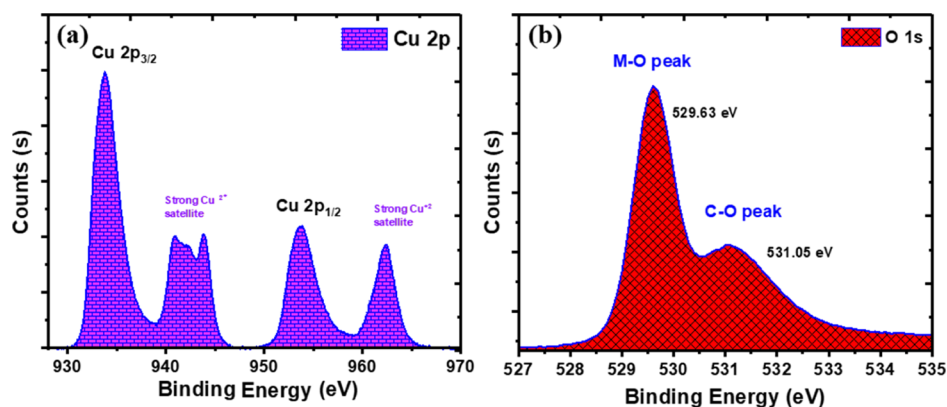
Figure 5. X-ray photoelectron spectral plots of (a) Cu 2p and (b) O 1s elements for RT synthesized CuO nanosheets.
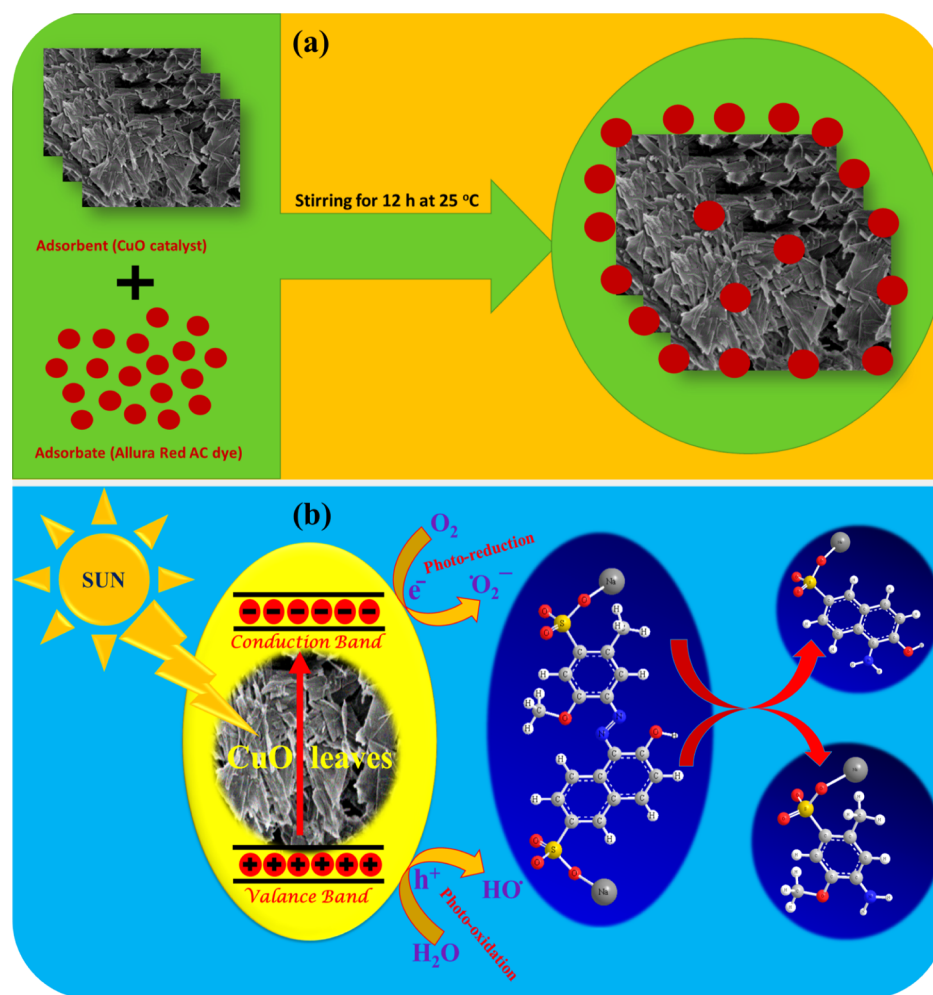

Figure 6. Proposed model presentation of the AR dye degradation mechanism by RT synthesized CuO nanosheets; (a) adsorption of the dye on CuO nanosheets and (b) catalytic degradation of the AR dye in the presence of light.

indicating the Cu^{2+} ionic state in pure CuO. The difference in binding energy between two characteristic peaks was calculated from spectra to be ~20.13 eV of the Cu spectrum.[46]

The O 1s spectra (Figure 5b) of CuO nanosheets display asymmetric peaks suggesting different chemical environments and at least two oxygen species of oxide ions. The strong peak at a binding energy of 529.63 eV is attributed to O^{2-} ions bonded to Cu^{2+} ions in the monoclinic crystal system. The additional broad peak at 531.05 eV might belong to vacant oxygen sites and

the surface-chemisorbed oxygen peak as H_2O or O_2 from the environment, resulting in weakly bonded oxygen species with CuO nanosheets.[47] The C 1s profiles (Figure S2) of CuO displayed a robust peak at 284.62 eV, indicating an sp^2-hybridized C−C carbon bond with a shoulder peak at 286.15 eV belonging to the C−O bond. Additionally, peaks at 287.98 eV are assigned to O−C=O or COOH groups, introduced by utilization of oxalic acid as a capping agent during the synthesis of the CuO catalyst.[48]
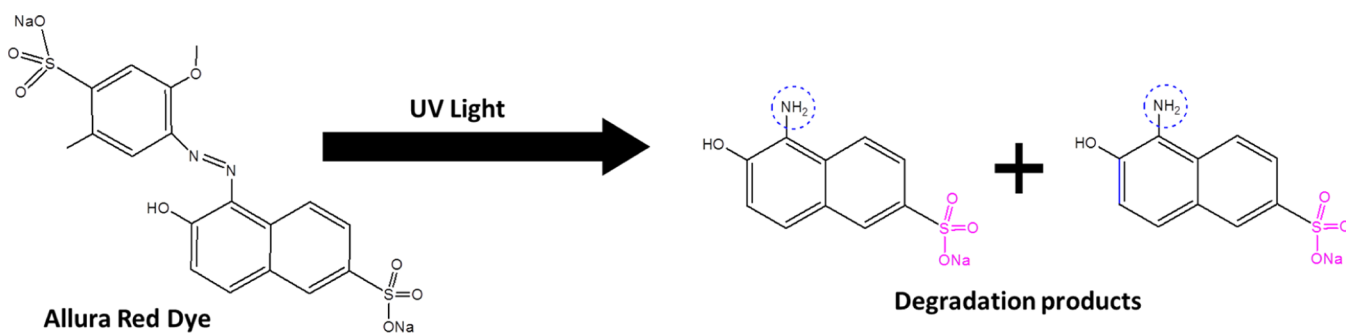
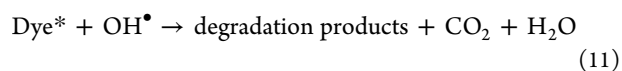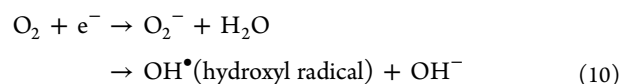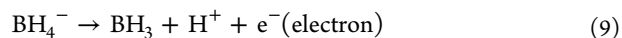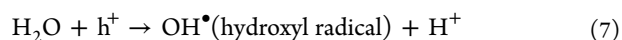**Figure 7.** Degradation products of the AR dye in the presence of the CuO catalyst.
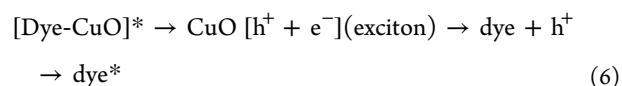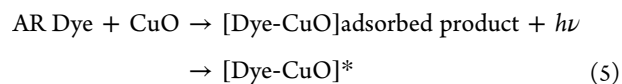
Brunauer−Emmet−Teller Surface Analysis of Porous CuO Nanosheets. It has been investigated that the obtained surface area of the CuO nanosheet catalyst is very high compared to the surface area of the commercial CuO powder (ca. 0.1 m^2/g) which revels a highly porous surface morphology and provides a large area to adsorb dye molecules, resulting in efficient and superfast degradation of the dye.[49] From Brunauer−Emmet−Teller (BET) investigation (Figure S3), RT grown CuO nanosheets exhibit a high surface area of ∼30.88 ± 0.2313 m^2/g, with an average pore size of ∼20.385 nm and an average pore volume of 0.146 cm^3/g. The highly porous structure of CuO nanosheets provides a bigger surface to facilitates mass transport during photodegradation reaction in aqueous solution. The porous CuO nanosheets have good crystalline nature and a clean surface without any bonding or adsorbing of surfactant molecules. However, in this work, CuO nanosheets provide a high surface area of ∼30 nm compared to the previous report.[50] Using the Barret-Joyner-Halenda (BJH) method, the values of pore volume and pore size show a highly mesoporous character of CuO nanosheets.[51] Specifically, the CuO catalyst displays a BJH adsorption average pore size (Figure S3 inset) of ∼19.37 nm and a desorption average pore size of ∼21.39 nm. For CuO nanosheets, the BJH adsorption and desorption pore volumes were estimated as ∼0.14113 and ∼0.15088 cm^3/g, respectively.

Proposed Mechanism of Photocatalytic Degradation of the Organic Pollutant/Dye Solutions. Owing to their complex aromatic structures, organic pollutants/dyes are very stable in aqueous solutions, which is a big concern for environmental water pollution. To remove organic pollutants, a tentative reaction mechanism (Figure 6) is proposed, which involves OH free radicals as active oxidizing agents during the photocatalytic process. During light-driven catalytic degradation, the band position of the catalyst determines the strength of the oxidation or reduction process. The catalyst nanomaterials are excited by light irradiation and form electron−hole pairs (e$^-$/h$^+$ pairs called excitons) which interact with hydride radicals (of the NaBH$_4$ reducing agent) to create a reactive oxygen species known as a superoxide (O$_2^-$) ion and hydroxyl free radicals.[52] The oxygen-containing radicals (O$_2^{-•}$ and HO$^•$) might react with electrons and holes to produce more hydroxyl radicals ($^•$OH), which derive photodegradation efficiency and enable ultrafast degradation of the AR dye under UV−vis light irradiation. The degradation process produces amine derivatives (colorless) which finally decompose to produce CO$_2$ and water.

To evaluate the effect of dye adsorption (Figure 6a) on the catalyst surface, the CuO catalyst was dissolved in the AR aqueous solution and stirred for 12 h at RT. When a freshly prepared aqueous solution of NaBH$_4$ was added to the AR solution in the absence of the CuO catalyst, no visible color change could be observed. Nevertheless, maximum absorption peak centered at ∼506 nm remained unaltered even after excessive addition of the NaBH$_4$ solution, which proved no degradation of the AR dye in the absence of the catalyst. At the chemical structural point, the presence of various functional groups in the AR dye can significantly affect photodegradation performance and yield of reaction.

The chromophore groups and azo bonds (−N=N−) in dyes are responsible for the red color and display a strong peak at a ∼506 nm wavelength due to n → π^* transition which is susceptible to photocatalytic degradation under UV light. At t = 0 min, UV absorption spectra of the AR solution with and without the CuO catalyst were recorded at RT. The degradation started with the addition of the NaBH$_4$ solution in terms of intensity decrease at RT. Hence, AR dye degradation (Figure 6b) might follow a possible breakage of the azo bond as the chromophoric group, which causes decolorization of the dye solution via the following steps

$$\text{AR Dye} + \text{CuO} \rightarrow [\text{Dye-CuO}]\text{adsorbed product} + h\nu$$
$$\rightarrow [\text{Dye-CuO}]^* \tag{5}$$

$$[\text{Dye-CuO}]^* \rightarrow \text{CuO }[h^+ + e^-](\text{exciton}) \rightarrow \text{dye} + h^+$$
$$\rightarrow \text{dye}^* \tag{6}$$

$$\text{H}_2\text{O} + h^+ \rightarrow \text{OH}^•(\text{hydroxyl radical}) + \text{H}^+ \tag{7}$$

$$\text{NaBH}_4 \rightarrow \text{Na}^+ + \text{BH}_4^- \tag{8}$$

$$\text{BH}_4^- \rightarrow \text{BH}_3 + \text{H}^+ + e^-(\text{electron}) \tag{9}$$

$$\text{O}_2 + e^- \rightarrow \text{O}_2^- + \text{H}_2\text{O}$$
$$\rightarrow \text{OH}^•(\text{hydroxyl radical}) + \text{OH}^- \tag{10}$$

$$\text{Dye}^* + \text{OH}^• \rightarrow \text{degradation products} + \text{CO}_2 + \text{H}_2\text{O} \tag{11}$$

During AR dye degradation, the CuO nanosheets displayed efficient catalytic activity with NaBH$_4$ as the reducing agent in aqueous solution. The process was monitored by UV−vis spectrophotometry at RT. The sodium borohydride (NaBH$_4$) reducing agent acts as a hydride ion source (to produce electrons), while CuO catalysts activate the azo bond of the AR dye via conjugation. Additionally, ultrafast dye degradation with CuO nanosheets might be due to additional electrons generated by BH$_4^-$ and efficient charge transfer by the CuO catalyst toward the AR dye.
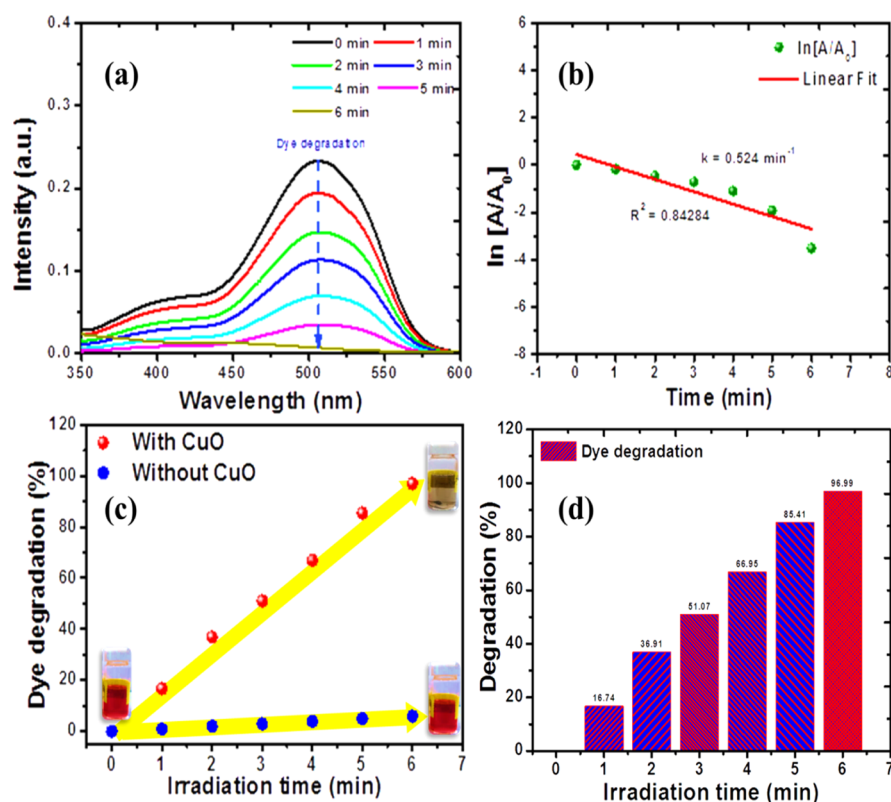
Figure 8. (a) UV−vis spectral plots of dye degradation at different time intervals and (b) corresponding reaction rate kinetic plot; (c) degradation percentage vs time curves of the AR dye with and without the CuO catalyst; (d) gradual degradation histogram profile against time of the AR dye in the aqueous medium.

The photodegradation reaction of the AR dye by CuO nanosheets was investigated using UV−vis absorption spectroscopy as gradual dye discoloration (lowering absorbance), measured as a function of time using Beer−Lambert's law. The AR dye gives degradation products (Figure 7) as amine derivatives (general formula, $C_8H_{10}NSNaO_4$, mol. wt: 239.22, and $C_{10}H_8NSNaO_4$, mol. wt: 261.23) which finally degrade into water and carbon dioxide on further photodegradation.

Catalytic Degradation of the AR Dye in the Aqueous Medium. The organic dye pollutant, namely, the AR dye, was chosen to investigate catalytic activity of CuO broken nanosheets under sunlight. To monitor the photocatalytic study of CuO nanostructures, 5 mg of prepared CuO nanostructures was dispersed in deionized water (10 mL) by sonication for 30 min. The AR dye solution (1 mg/10 mL) was added separately into the CuO dispersed solution and stirred for 12 h at RT to attain an adsorption−desorption equilibrium of CuO and the AR dye. The photocatalytic degradation reaction (Figure 8) of the organic pollutant started with the addition of the $NaBH_4$ (1 mg/mL) solution as a reducing agent. In the absence of CuO nanostructures, the absorption peak intensity remained the same after the addition of the reducing agent, $NaBH_4$. On light exposure, the main absorbance peak at ~506 nm from the azo groups in the AR dye gradually decreases, which can be evaluated to determine the PE (Table 2) of CuO nanosheets. The absorption peak intensity remains the same after the addition of the reducing agent, $NaBH_4$, in the absence of CuO nanostructures. Due to the large kinetic barrier, the rate of dye photodegradation is extremely slow and negligible in the absence of the CuO nanocatalyst besides a thermodynamically favorable reaction.[53] After a specific time interval, a 2 mL sample

Table 2. Photocatalytic Efficiency and Reaction Kinetic Parameters of the AR Dye Solution

dye	rate constant (k, min^{-1})	half-life ($t_{1/2}$) (min)	PE (%)	degradation time (min)
AR dye	0.524	2.5	96.99	6

solution was collected and centrifuged to remove the catalyst and then analyzed using UV−vis spectroscopy. The removal of the organic pollutants/dye (Figure S4) was apparent and confirmed by conversion of the dye solution (red color) to a degraded dye (colorless solution). Due to the strong quantum size confinement effect, CuO nanosheets exhibited high band gap energy, high crystallinity, and eminent photocatalytic activity for instant photodegradation of organic pollutants.[54]

■ CATALYTIC EFFICIENCY OF POROUS CUO NANOSHEETS AS A PHOTOCATALYST

The possible mechanism of excellent catalytic performance of RT synthesized CuO nanosheets is attributed to high adsorption ability toward AR via the high BET surface area and high porosity along with the large pore size compared to commercial CuO powder. Owing to high nucleophilicity, BH_4^- anions supply more electrons to enhance dye degradation reaction.[55] In addition, high dispersing ability of the CuO catalyst in water also results in highly efficient contact between CuO nanosheets and the AR dye. The enhanced PE of CuO might be due to shift in light absorption toward the visible range, resulting in an increase of optical band gap. During photocatalytic degradation, oxygen sites appeared on CuO nanosheets which reduce O_2 and form superoxide radicals, resulting in the ultrafast photocatalytic degradation of the organic pollutants in the aqueous medium.

The photocatalytic degradation efficiency (Figure 8a) of RT synthesized CuO nanosheets as a catalyst was observed with absorbance variation at the maximum wavelength (λ_{max}) peak of the AR dye at different time intervals. The AR dye solution exhibited the highest-intensity absorption peak at ~506 nm, along with two low-intensity peaks at ~315 and ~405 nm in water. According to the Beer–Lambert law, the PE of CuO nanosheets can be calculated using following equation

$$\text{Photocatalytic efficiency (\%)} = (1 - A_t/A_0) \times 100 \tag{12}$$

where A_0 represents the absorbance of the AR dye aqueous solution at time $t = 0$ and A_t is the absorbance of the dye aqueous solution after time t of photoirradiation. Due to the addition of the CuO nanocatalyst, the absorption intensity of the azo dye declines with cleavage of azo bonds, producing colorless amino derivatives. On UV light irradiation, the AR dye was efficiently degraded by the CuO nanosheet photocatalyst and a PE of ~96.99% (Table 2) was evaluated in 6 min at RT. Additionally, ultrafast decolorization of the dye was evidenced by disappearance of the maximum intensity peak at 506 nm wavelength. The superfast organic pollutant/dye degradation was attributed to superior electron-transfer ability and the effective light harvesting tendency of CuO nanosheets.[56]

REACTION KINETICS OF PHOTOCATALYTIC DEGRADATION OF THE ORGANIC POLLUTANT/AR DYE

Generally, a large redox potential barrier between the electron-donor (BH_4^-) ion and electron acceptor (dyes) kinetically suppresses rapid degradation of the AR dye in aqueous solution. RT synthesized CuO nanosheets might improve electron transfer owing to the large surface for dye adsorption via an electrostatic attraction to boost desirable photodegradation reactions within a few minutes.

In addition, the presence of excess NaBH$_4$ during photodegradation reactions establishes a pseudo-first-order kinetic mechanism using the Langmuir–Hinshelwood model (Figure 8b) for AR dye degradation.[57] Due to the linear relation of AR dye degradation, the photodegradation rate constant, k, can be calculated as follows

$$\ln(A_t/A_0) = -kt \tag{13}$$

where k is the pseudo-first-order rate constant and A_t and A_0 are the corresponding absorbance values of the AR dye solution at time t and 0 min, respectively. During the photocatalytic process, the absorbance change (A_t/A_0) of the AR solution appears to be directly proportional to concentration change (C_t/C_0) which can be derived from the Beer–Lambert law. In this work, the linear fit curve of $\ln(A/A_0)$ versus time (t, min) plots (Figure 8b) established that degradation of AR undergoes a pseudo-first-order reaction kinetics.

When RT synthesized CuO nanosheets were used as a photocatalyst, the rate constant (k) of the photodegradation reaction of the AR dye was calculated to be 0.524 min^{-1}. The high PE of CuO can be attributed to the high band gap and the porous sheetlike morphology, which enhances dye adsorption capacity. Additionally, the half-life ($t_{1/2}$) of the degradation reactions (Figure 8c,d) was also estimated in the presence and absence of the CuO photocatalyst in terms of $(\ln 2)/k$ relation. The photodegradation of the dye with CuO nanosheets exhibited a low value of $t_{1/2}$ (~2.5 min), revealing the strong PE of CuO nanosheets compared to the high $t_{1/2}$ value of 36.6

min (Table 2) for photodegradation reaction without the CuO catalyst.[58]

Reusability of the CuO Catalyst. The reusability and recovery of the catalyst CuO after the photocatalytic experiment are crucial and important features during research. The CuO catalyst could be readily separated from the reaction mixture and makes it possible to reuse CuO nanosheets. From Figure S5, CuO catalysts retained their original catalytic activity even after 10 cycles, which indicates good stability (>90%) of the CuO catalyst.[59] Furthermore, the CuO catalyst was recovered from the reaction mixture at the end of each process, washed with water and ethanol, dried in a vacuum oven, and then characterized for XRD (Figure S6a) and FESEM images (Figure S6b) for storage to apply in next degradation cycles at ambient temperature. From Figure S5, CuO catalysts retained their original catalytic activity even after 10 cycles, which indicates good stability (>90%) of the CuO catalyst.[60] Therefore, good catalytic efficiency, good stability, and facile recycling ability of RT synthesized CuO made the catalyst promising for environmental remediation.

CONCLUSIONS

In summary, we have demonstrated the facile, environmentally friendly RT synthesis of porous CuO broken nanosheets and applied them as catalysts to degrade the organic pollutant/food dye, the AR dye using NaBH$_4$ as a reducing agent in aqueous solution. The UHR–FESEM images revealed a broken nanosheet-like morphology (a length up to ~160 nm, a width up to ~65 nm). The strain of CuO nanosheets was estimated to be ~1.24 × 10^{-3} using Williamson–Hall analysis from XRD spectra. The CuO nanosheets exhibited a high optical energy band gap of ~1.92 eV due to the strong quantum size confinement effect, as determined by using Tauc plots. The Raman spectral plots exhibited three strong peaks at 270, 335, and 597 cm^{-1}, which were assigned to the monoclinic orientation of the A$_{1g}$, B$_{1g}$, and B$_g$ vibrational modes of CuO nanosheets, respectively. From XRD plots, the obtained CuO nanosheets exhibited a high crystallinity of 73.5% with a crystallite size of ~12 nm. The RT synthesized CuO catalyst showed a high BET surface area of 30.88 ± 0.2313 m^2/g (a correlation coefficient of 0.9997268) with an average BJH pore size of ~20.385 nm. From UV–vis spectra, the PE of RT synthesized CuO nanosheets exhibited an efficient and ultrafast dye degradation of ~96.99% for the AR dye in 6 min. According to the Langmuir–Hinshelwood model, dye degradation reaction kinetics followed a pseudo-first-order reaction, with a rate constant of $k = 0.524$ min^{-1}, with a half-life ($t_{1/2}$) of 2.5 min for AR dye degradation reaction.
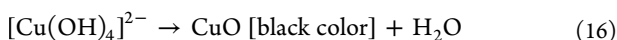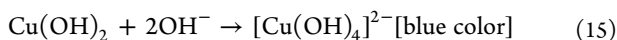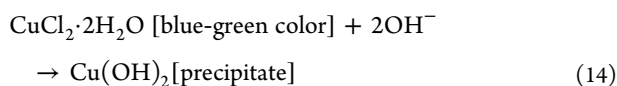
EXPERIMENTAL SECTION

Materials and Methods. All the abovementioned chemicals were of analytical grade and were used without any further purification. Copper chloride dihydrate (CuCl$_2$·2H$_2$O), sodium hydroxide (NaOH), and oxalic acid dihydrate were all purchased from Sigma-Aldrich, Korea. During experiments, deionized water was used to make up aqueous solutions of various components.

Characterizations. UHR–FESEM images of CuO nanosheets were obtained with a Hitachi (SU 8230) instrument using fine powder, along with their elemental mapping images. EDX was employed to evaluate the weight percent of various elements. During degradation, UV–vis spectra of the AR dye

(quartz cuvette) solutions were recorded using a Cary 5000 UV−vis−NIR spectrophotometer (Agilent Technologies) with D2 and tungsten lamps in the range of 200−800 nm wavelengths. At RT, UV absorption spectra were calibrated against deionized water as the background in the same quartz cuvette. HR-XRD spectra were recorded in the range of 5−80° with Cu Kα radiation (λ = 1.5406 Å) using an X-ray diffractometer (Empyrean, Panalytical, USA) to analyze structural properties of the CuO nanosheet powder. The elemental composition of CuO nanosheets was measured using X-ray photoelectron spectroscopic analysis in an ultrahigh vacuum setup equipped with a monochromatic Al Kα X-ray source (1486.6 eV) (ESCALAB 250Xi, Thermo Fisher Scientific, USA) at RT. HR−TEM (S-4800, Hitachi, Japan) was employed to examine the atomic structure and various lattice planes of the CuO powder, and the lattice d-spacing value was calculated by FFT patterns of TEM images. FT-IR spectroscopy (Nicolet Continuum, Thermo Fisher Scientific, USA) was performed in the attenuated total reflectance mode at a resolution of 4 cm^{-1}. FT-IR spectra of CuO were recorded in range of 4000−650 cm^{-1} at RT. Raman spectroscopy was performed using a confocal Raman spectrometer (Thermo Fisher Scientific, Nicolet Almeca XRA) with a λ_{ex} of 532 nm at RT. The photocatalytic activity of CuO for degradation of the AR dye was evaluated at ambient temperature using a UV−vis−NIR spectrophotometer.

RT Synthesis of CuO Nanosheets. At RT, copper chloride dihydrate (CuCl$_2$·2H$_2$O, 2 mmol) and sodium hydroxide (NaOH, 20 mmol) were dissolved (1:10 molar ratio) in 50 mL of deionized water (Figure 1) and stirred for 15 min to get a homogeneous blue-colored solution. The reaction progress was monitored through naked eyes, and the reaction mixture changed from blue green to blue. Then, oxalic acid dihydrate (4 mmol) was added as a capping agent slowly in the reaction mixture with constant stirring at RT. The reaction mixture was stirred for 30 min and converted into a black suspension. Furthermore, Cu^{2+} ions can react with OH$^-$ ions to produce a Cu(OH)$_2$ precipitate.[60] However, excess OH$^-$ ions react with copper ions to form a blue solution of [Cu(OH)$_4$]$^{2-}$ complex ions which convert into CuO as follows

$$CuCl_2 \cdot 2H_2O \text{ [blue-green color]} + 2OH^-$$
$$\rightarrow Cu(OH)_2 \text{[precipitate]} \tag{14}$$

$$Cu(OH)_2 + 2OH^- \rightarrow [Cu(OH)_4]^{2-} \text{[blue color]} \tag{15}$$

$$[Cu(OH)_4]^{2-} \rightarrow CuO \text{ [black color]} + H_2O \tag{16}$$

The synthesized CuO nanosheets were separated by centrifugation at 6000 rpm for 10 min at RT. The reaction mixture was filtered and thoroughly washed with ethanol and deionized water several times. The raw solid powder was then dried at 60 °C for 1 h to get pure CuO nanosheets as a black powder.

Catalytic Experiments. The organic food dye, namely, AR, was chosen to investigate catalytic activity of RT grown CuO nanosheets at RT. For degradation reaction, 10 mL of the aqueous solution of the dye (5 mg L^{-1}) was added with a freshly prepared NaBH$_4$ (1 mg/mL) solution to record the peak intensity under UV−visible spectra. Immediately, the preferred amount of catalyst was added to precede degradation reaction which can be observed by color change of the solution from red to colorless with stirring solution. The supernatant was then

transferred to a quartz cuvette for the UV−vis spectral measurement. After the UV spectrum was recorded, the solution was transferred back to the previous reaction vessel while stirring. The process was repeated and UV−visible spectra were recorded consecutively to check the progress of the reaction. In addition, blank experiments were also conducted to confirm that reactions did not proceed with the catalyst in the absence of NaBH$_4$ or without the catalyst in the presence of NaBH$_4$. The influence of catalyst amount and reusability of the CuO catalyst were investigated for degradation reaction. To test reusability, 10 consecutive cycles of the catalyst were carried out with a fixed amount of the catalyst. In consecutive cycles, the catalyst was recovered by centrifugation, followed by washing with distilled water three times, and characterized by XRD and FESEM of CuO nanosheets. Further, the recovered catalyst was employed against the fresh reaction mixture, as described previously.

■ ASSOCIATED CONTENT

ⓈⒾ Supporting Information
The Supporting Information is available free of charge at https://pubs.acs.org/doi/10.1021/acsomega.0c04747.

> Williamson−Hall plots, XPS plots, BET surface area plots, reusability plots of 10 cycles, and XRD and FESEM images of CuO nanosheets after 10 degradation cycles of the AR dye (PDF)

■ AUTHOR INFORMATION

Corresponding Authors
Mohammed Nazim − *Division of Energy Technology, Daegu Gyeongbuk Institute of Science & Technology (DGIST), Daegu 42988, Republic of Korea;* ⓞ orcid.org/0000-0002-3391-2677; Email: nazimopv@gmail.com
Jae Hyun Kim − *Division of Energy Technology, Daegu Gyeongbuk Institute of Science & Technology (DGIST), Daegu 42988, Republic of Korea;* ⓞ orcid.org/0000-0003-2824-0113; Email: jaehyun@dgist.ac.kr

Authors
Aftab Aslam Parwaz Khan − *Chemistry Department, Faculty of Science, King Abdulaziz University, Jeddah 21589, Saudi Arabia;* ⓞ orcid.org/0000-0002-3746-5034
Abdullah M. Asiri − *Chemistry Department, Faculty of Science and Center of Excellence for Advanced Materials Research, King Abdulaziz University, Jeddah 21589, Saudi Arabia*

Complete contact information is available at:
https://pubs.acs.org/10.1021/acsomega.0c04747

Notes
The authors declare no competing financial interest.

■ REFERENCES

(1) Ren, Z. J.; Umble, A. K. Water treatment: Recover wastewater resources locally. *Nature* **2016**, *529*, 316−325.

(2) Sha, Y.; Mathew, I.; Cui, Q.; Clay, M.; Gao, F.; Zhang, X. J.; Gu, Z. Rapid degradation of azo dye methyl orange using hollow cobalt nanoparticles. *Chemosphere* **2016**, *144*, 1530−1535.

(3) Li, W.-W.; Yu, H.-Q.; Rittmann, B. E. Chemistry: Reuse water pollutants. *Nature* **2015**, *528*, 29−31.

(4) dos Santos, A. B.; Cervantes, F. J.; van Lier, J. B. Review paper on current technologies for decolourisation of textile wastewaters: Perspectives for anaerobic biotechnology. *Bioresour. Technol.* **2007**, *98*, 2369−2385.

(5) Lasio, B.; Malfatti, L.; Innocenzi, P. Photodegradation of Rhodamine 6G dimers in silica sol-gel films. *J. Photochem. Photobiol., A* **2013**, *271*, 93−98.

(6) Buthiyappan, A.; Abdul Aziz, A. R.; Wan Daud, W. M. A.; Daud, W. Recent advances and prospects of catalytic advanced oxidation process in treating textile effluents. *Rev. Chem. Eng.* **2016**, *32*, 1−47.

(7) Arslan, I.; Balcioğlu, I. A. Degradation of commercial reactive dyestuffs by heterogenous and homogenous advanced oxidation processes: a comparative study. *Dyes Pigment* **1999**, *43*, 95−108.

(8) Cooper, P. Removing color from dye house waste waters-A critical review of technology available. *J. Soc. Dyers Color.* **1993**, *109*, 97−100.

(9) Pagga, U.; Taeger, K. Development of a method for adsorption of dyestuffs on activated sludge. *Water Res.* **1994**, *28*, 1051−1057.

(10) Forgacs, E.; Cserháti, T.; Oros, G. Removal of synthetic dyes from wastewaters: a review. *Environ. Int.* **2004**, *30*, 953−971.

(11) Wongrakpanich, A.; Mudunkotuwa, I. A.; Geary, S. M.; Morris, A. S.; Mapuskar, K. A.; Spitz, D. R.; Grassian, V. H.; Salem, A. K. Size-dependent cytotoxicity of copper oxide nanoparticles in lung epithelial cells. *Environ. Sci.: Nano* **2016**, *3*, 365−374.

(12) Salem, M. A.; Al-Ghonemiy, A. F.; Zaki, A. B. Photocatalytic degradation of Allura red and Quinoline yellow with polyaniline/TiO₂ nanocomposite. *Appl. Catal., B* **2009**, *91*, 59−66.

(13) Wang, Y.; Wang, D.; Yan, B.; Chen, Y.; Song, C. Fabrication of diverse CuO nanostructures via hydrothermal method and their photocatalytic properties. *J. Mater. Sci.: Mater. Electron.* **2016**, *27*, 6918−6924.

(14) Saadati, F.; Khani, N.; Rahmani, M.; Piri, F. Preparation and characterization of nanosized copper (II) oxide embedded in hyper-cross-linked polystyrene: highly efficient catalyst for aqueous-phase oxidation of aldehydes to carboxylic acids. *Catal. Commun.* **2016**, *79*, 26−30.

(15) Wang, Y.; Jiang, T.; Meng, D.; Yang, J.; Li, Y.; Ma, Q.; Han, J. Fabrication of nanostructured CuO films by electrodeposition and their photocatalytic properties. *Appl. Surf. Sci.* **2014**, *317*, 414−421.

(16) Andrews, B.; Almahdali, S.; James, K.; Ly, S.; Crowder, K. N. Copper oxide surfaces modified by alkylphosphonic acids with terminal pyridyl-based ligands as a platform for supported catalysis. *Polyhedron* **2016**, *114*, 360−369.

(17) Shu, H.-Y.; Chang, M.-C.; Yu, H.-H.; Chen, W.-H. Reduction of an azo dye Acid Black 24 solution using synthesized nanoscale zerovalent iron particles. *J. Colloid Interface Sci.* **2007**, *314*, 89−97.

(18) Chani, M. T. S.; Karimov, K. S.; Khan, S. B.; Asiri, A. M. Fabrication and investigation of cellulose acetate-copper oxide nano-composite based humidity sensors. *Sens. Actuators, A* **2016**, *246*, 58−65.

(19) Wu, D.; Yan, J.; Wang, J.; Wang, Q.; Li, H. Characterisation of interaction between food colourant allura red AC and human serum albumin: Multispectroscopic analyses and docking simulations. *Food Chem.* **2015**, *170*, 423−429.

(20) Tsuda, S.; Murakami, M.; Matsusaka, N.; Kano, K.; Taniguchi, K.; Sasaki, Y. F. DNA damage induced by red food dyes orally administered to pregnant and male mice. *Toxicol. Sci.* **2001**, *61*, 92−99.

(21) Zhong, Y.; Shi, T.; Liu, Z.; Cheng, S.; Huang, Y.; Tao, X.; Liao, G.; Tang, Z. Ultrasensitive non-enzymatic glucose sensors based on different copper oxide nanostructures by in-situ growth. *Sens. Actuators, B* **2016**, *236*, 326−333.

(22) Amchova, P.; Kotolova, H.; Ruda-Kucerova, J. Health safety issues of synthetic food colorants. *Regul. Toxicol. Pharmacol.* **2015**, *73*, 914−922.

(23) Li, K.; Lu, J.; Zheng, X.; Lian, Q. Three-dimensional hierarchical superstructures of CuO nanoflowers: Facile synthesis and applications for enhanced photocatalytic activity of dyes. *Russian J. Appl. Chem.* **2019**, *92*, 71−77.

(24) Honma, M. Evaluation of the *in vivo* genotoxicity of Allura red AC (Food Red No. 40). *Food Chem. Toxicol.* **2015**, *84*, 270−275.

(25) Tang, W. Z.; Huren An, H. UV/TiO₂ photocatalytic oxidation of commercial dyes in aqueous solutions. *Chemosphere* **1995**, *31*, 4157−4170.

(26) Wang, H.; Pan, Q.; Zhao, J.; Chen, W. Fabrication of CuO/C films with sisal-like hierarchical microstructures and its application in lithium ion batteries. *J. Alloys Compd.* **2009**, *476*, 408−413.

(27) Li, F.; Liu, X.; Zhang, Q.; Kong, T.; Jin, H. Fabrication and photocatalytic property of CuO nanosheets via a facile solution route. *Cryst. Res. Technol.* **2012**, *47*, 1140−1147.

(28) Yamamoto, K.; Kasuga, T.; Nogami, M. Electrochemical Reactions of a Novel Oxygen Sensor Using Copper(I)-Conducting Glass-Ceramics. *Electrochem. Solid State Lett.* **1999**, *2*, 595−596.

(29) Gao, X. P.; Bao, J. L.; Pan, G. L.; Zhu, H. Y.; Huang, P. X.; Wu, F.; Song, D. Y. Preparation and electrochemical performance of polycrystalline and single crystalline CuO nanorods as anode materials for Li ion battery. *J. Phys. Chem. B* **2004**, *108*, 5547−5551.

(30) Rao, M. P.; Wu, J. J.; Asiri, A. M.; Anandan, S.; Ashokkumar, M. Photocatalytic properties of hierarchical CuO nanosheets synthesized by a solution phase method. *J. Environ. Sci.* **2018**, *69*, 115−124.

(31) Kosa, S. A.; Maksod, I. H. A. E.; Alkhateeb, L.; Hegazy, E. Z.; Hegazy, E. Z. Preparation and surface characterization of CuO and Fe2O3 catalyst. *App. Surf. Sci.* **2012**, *258*, 7617−7624.

(32) Sankar, R.; Manikandan, P.; Malarvizhi, V.; Fathima, T.; Shivashangari, K. S.; Ravikumar, V. Green synthesis of colloidal copper oxide nanoparticles using Carica-papaya and its application in photocatalytic dye degradation. *Spectrochim. Acta, Part A* **2014**, *121*, 746−750.

(33) Wang, H.; Pan, Q.; Zhao, J.; Yin, G.; Zuo, P. Fabrication of CuO film with network-like architectures through solution-immersion and their application in lithium ion batteries. *J. Power Sources* **2007**, *167*, 206−211.

(34) Zhang, Q.; Zhang, K.; Xu, D.; Yang, G.; Huang, H.; Nie, F.; Liu, C.; Yang, S. CuO nanostructures: Synthesis, characterization, growth mechanisms, fundamental properties, and applications. *Prog. Mater. Sci.* **2014**, *60*, 208−337.

(35) Yao, Y.; Chen, H.; Qin, J.; Wu, G.; Lian, C.; Zhang, J.; Wang, S. Iron encapsulated in boron and nitrogen codoped carbon nanotubes as synergistic catalysts for Fenton-like reaction. *Water Res.* **2016**, *101*, 281−291.

(36) Baskoutas, S.; Terzis, A. F. Size-dependent band gap of colloidal quantum dots. *J. Appl. Phys.* **2006**, *99*, 013708−13711.

(37) Rehman, S.; Ullah, R.; Butt, A. M.; Gohar, N. D. Strategies of making TiO₂ and ZnO visible light active. *J. Hazard. Mater.* **2009**, *170*, 560−569.

(38) Erdoğan, I. Y.; Güllü, Ö. Optical and structural properties of CuO nanofilm: Its diode application. *J. Alloy. Compd.* **2010**, *492*, 378−383.

(39) Kana, N.; Kaviyarasu, K.; Khamliche, T.; Magdalane, C. M.; Maaza, M. Stability and thermal conductivity of CuO nanowire for catalytic applications. *J. Environ. Chem. Engg.* **2019**, *7*, 103255.

(40) Qasem, M.; El Kurdi, R.; Patra, D. Green synthesis of Curcumin conjugated CuO nanoparticles for catalytic reduction of Methylene Blue. *Chem. Select* **2020**, *5*, 1694−1704.

(41) Uthirakumar, P.; Muthulingam, S.; Khan, R.; Hyeon Yun, J.; Cho, H.-S.; Lee, I.-H. Surfactant-free synthesis of leaf-like hierarchical CuO nanosheets as a UV light filter. *Mater. Lett.* **2015**, *156*, 191−194.

(42) Mukherjee, N.; Show, B.; Maji, S. K.; Madhu, U.; Bhar, S. K.; Mitra, B. C.; Khan, G. G.; Mondal, A. CuO nano-whiskers: electrodeposition, Raman analysis, photoluminescence study and photocatalytic activity. *Mater. Lett.* **2011**, *65*, 3248−3250.

(43) Xu, H.-Y.; Liu, W.-C.; Qi, S.-Y.; Li, Y.; Zhao, Y.; Li, J.-W. Kinetics and optimization on discoloration of dyeing wastewater by schorl-catalyzed Fenton-like reaction. *J. Serb. Chem. Soc.* **2014**, *79*, 361−377.

(44) Wang, Y.; Lü, Y.; Zhan, W.; Xie, Z.; Kuang, Q.; Zheng, L. Synthesis of porous Cu_2O/CuO cages using Cu-based metal−organic frameworks as templates and their gas-sensing properties. *J. Mater. Chem. A* **2015**, *3*, 12796−12803.

(45) Wu, C.-K.; Yin, M.; O'Brien, S.; Koberstein, J. T. Quantitative analysis of copper oxide nanoparticle composition and structure by X-ray photoelectron spectroscopy. *Chem. Mater.* **2006**, *18*, 6054−6058.

(46) Yang, F.; Zhang, X.; Yang, Y.; Hao, S.; Cui, L. Characteristics and supercapacitive performance of nanoporous bamboo leaf-like CuO. *Chem. Phys. Lett.* **2018**, *691*, 366−372.

(47) Zhong, K.; Xue, J.; Mao, Y.; Wang, C.; Zhai, T.; Liu, P.; Xia, X.; Li, H.; Tong, Y. Facile synthesis of CuO nanorods with abundant adsorbed oxygen concomitant with high surface oxidation states for CO oxidation. *RSC Adv.* **2012**, *2*, 11520−11528.

(48) Liu, S.; Wang, Z.; Wang, F.; Yu, B.; Zhang, T. High surface area mesoporous CuO: a high-performance electrocatalyst for non-enzymatic glucose biosensing. *RSC Adv.* **2014**, *4*, 33327−33331.

(49) Xu, H.; Zhu, G.; Zheng, D.; Xi, C.; Xu, X.; Shen, X. Porous CuO superstructure: Precursor-mediated fabrication, gas sensing and photocatalytic properties. *J. Colloid Interface Sci.* **2012**, *383*, 75−81.

(50) Zou, G.; Li, H.; Zhang, D.; Xiong, K.; Dong, C.; Qian, Y. Well-Aligned arrays of CuO nanoplatelets. *J. Phys. Chem. B* **2006**, *110*, 1632−1637.

(51) Dörner, L.; Cancellieri, C.; Rheingans, B.; Walter, M.; Kägi, R.; Schmutz, P.; Kovalenko, M. V.; Jeurgens, L. P. H. Cost-effective sol-gel synthesis of porous CuO nanoparticle aggregates with tunable specific surface area. *Sci. Rep.* **2019**, *9*, 11758.

(52) Fuku, X.; Kaviyarasu, K.; Matinise, N.; Maaza, M. Punicalagin green functionalized Cu/Cu_2O/ZnO/CuO nanocomposite for potential electrochemical transducer and catalyst. *Nanoscale Res. Lett.* **2016**, *11*, 386.

(53) Harish, S.; Sabarinathan, R.; Joseph, J.; Phani, K. L. N. Role of pH in the synthesis of 3-aminopropyl trimethoxysilane stabilized colloidal gold/silver and their alloy sols and their application to catalysis. *Mater. Chem. Phys.* **2011**, *127*, 203−207.

(54) Azad, U. P.; Ganesan, V.; Pal, M. Catalytic reduction of organic dyes at gold nanoparticles impregnated silica materials: Influence of functional groups and surfactants. *J. Nanopart. Res.* **2011**, *13*, 3951−3959.

(55) Nemanashi, M.; Meijboom, R. Synthesis and characterization of Cu, Ag and Au dendrimer-encapsulated nanoparticles and their application in the reduction of 4-nitrophenol to 4-aminophenol. *J. Colloid Interface Sci.* **2013**, *389*, 260−267.

(56) Miyajima, M.; Sagami, I.; Daff, S.; Taiko Migita, C.; Shimizu, T. Azo reduction of Methyl Red by neuronal nitric oxide synthase: The important role of FMN in catalysis. *Biochem. Biophys. Res. Commun.* **2000**, *275*, 752−758.

(57) Zhang, D.; Mai, H.; Huang, L.; Shi, L. Pyridine-thermal synthesis and high catalytic activity of CeO_2/CuO/CNT nanocomposites. *Appl. Surf. Sci.* **2010**, *256*, 6795−6800.

(58) Wang, J.; Fan, X. M.; Wu, D. Z.; Dai, J.; Liu, H.; Liu, H. R.; Zhou, Z. W. Fabrication of CuO/T-ZnOw nanocomposites using photo-deposition and their photocatalytic property. *Appl. Surf. Sci.* **2011**, *258*, 1797−1805.

(59) Akram, N.; Guo, J.; Ma, W.; Guo, Y.; Hassan, A.; Wang, J. Synergistic catalysis of $Co(OH)_2$/CuO for the degradation of organic pollutant under visible light irradiation. *Sci. Rep.* **2020**, *10*, 1939.

(60) Bhosale, M. A.; Karekar, S. C.; Bhanage, B. M. Room Temperature Synthesis of Copper Oxide Nanoparticles: Morphological Evaluation and Their Catalytic Applications for Degradation of Dyes and C-N Bond Formation Reaction. *ChemistrySelect* **2016**, *1*, 6297−6307.